

Node-Oriented Proactive Spectral Modulation: A Unified Fractional Framework for Graph Signal Denoising

Manjun Cui, Zhichao Zhang, *Member, IEEE*, and Yangfan He

Abstract—Graph signal denoising is a fundamental task in graph signal processing. While the node-oriented filtering approach enhances spatial adaptability, it suffers from spectral rigidity due to its reliance on the graph Fourier transform. Conversely, emerging fractional-domain transforms provide crucial spectral flexibility but are fundamentally limited by their globally shared filtering paradigm, failing to accommodate localized topological variations. To bridge this gap, this paper proposes a generalized node-oriented fractional filtering (NOFF) framework that seamlessly integrates localized spatial adaptability with proactive spectral modulation across various fractional transforms. However, straightforwardly assigning independent full-rank filters to all vertices incurs a prohibitive parameter space, leading to severe overfitting on random noise. To mitigate this, we introduce the low-rank NOFF (LRNOFF) architecture. By imposing a strict low-rank constraint, LRNOFF inherently acts as a powerful implicit regularizer, preventing noise memorization and ensuring the extraction of robust spectral bases. Furthermore, we develop an efficient computational implementation termed LRNOFF-Fast, which drastically reduces computational and memory overhead while preserving theoretical optimality. Experiments on real-world datasets demonstrate that the proposed framework achieves state-of-the-art performance.

Index Terms—Fractional-domain transforms, graph signal denoising, low-rank approximation, node-oriented filtering.

I. INTRODUCTION

In recent years, data generated from diverse real-world applications, such as sensor networks, transportation systems, social media, and biological networks, are increasingly represented on irregular, non-Euclidean domains. To effectively analyze such complex data, graph signal processing (GSP) has emerged as a powerful and unified mathematical framework by extending classical SP concepts to graph-structured data [1], [2]. GSP has demonstrated

This work was supported in part by the Open Foundation of Hubei Key Laboratory of Applied Mathematics (Hubei University) under Grant HBAM202404; in part by the Foundation of Key Laboratory of System Control and Information Processing, Ministry of Education under Grant Scip20240121; in part by the Startup Foundation for Introducing Talent of Nanjing Institute of Technology under Grant YKJ202214; and in part by the Open Foundation of Jiangsu Province Engineering Research Center of IntelliSense Technology and System under Grant ITS202502. (*Corresponding author: Zhichao Zhang.*)

Manjun Cui is with the School of Mathematics and Statistics, Nanjing University of Information Science and Technology, Nanjing 210044, China (e-mail: cmj1109@163.com).

Zhichao Zhang is with the School of Mathematics and Statistics, Nanjing University of Information Science and Technology, Nanjing 210044, China, with the Hubei Key Laboratory of Applied Mathematics, Hubei University, Wuhan 430062, China, and also with the Key Laboratory of System Control and Information Processing, Ministry of Education, Shanghai Jiao Tong University, Shanghai 200240, China (e-mail: zzc910731@163.com).

Yangfan He is with the School of Communication and Artificial Intelligence, School of Integrated Circuits, Nanjing Institute of Technology, Nanjing 211167, China, and also with the Jiangsu Province Engineering Research Center of IntelliSense Technology and System, Nanjing 211167, China (e-mail: Yangfan.He@njit.edu.cn).

remarkable efficacy in a multitude of fundamental tasks, including signal reconstruction, sampling, semi-supervised classification, and prediction [3]–[8]. Among these tasks, graph signal denoising plays a foundational and indispensable role [9]–[12]. Since real-world graph signals collected from physical environments are inevitably corrupted by measurement errors, sensing anomalies, or transmission noise, effective denoising serves as a critical preprocessing step that fundamentally dictates the performance and reliability of downstream analysis and graph representation learning.

In GSP, the graph Fourier transform (GFT) provides the fundamental spectral tools for graph signal denoising [13]–[16]. By mapping signals into the graph spectral domain, denoising can be achieved by designing specific spectral responses, such as low-pass or band-pass filters. A fundamental premise of these conventional approaches is that the filters are globally shared, meaning an identical spectral response is rigidly applied to all vertices across the entire graph. However, real-world graph data typically exhibit spatial irregularity, structural heterogeneity, and localized varying patterns. Consequently, a globally shared filter suffers from a one-size-fits-all limitation. It is fundamentally incapable of accommodating the highly varying local neighborhood topologies, thereby severely restricting its representational capacity and denoising efficacy in regions with complex structural characteristics.

To overcome the limitations of global filtering, recent advances have introduced the concept of node-oriented graph filtering, which assigns customized spectral responses to individual vertices [17]. By providing independent and flexible spectral weights for different nodes, this paradigm significantly enhances spatial adaptability, enabling a more accurate modeling of localized topological variations and node-specific characteristics. Consequently, it has demonstrated remarkable empirical success in complex graph representation learning tasks, particularly in semi-supervised node classification on graphs with severe heterophily [17]. However, despite this spatial flexibility, the node-oriented method is predominantly established upon the standard GFT domain, thereby restricting the spectral representational capacity to a rigidly fixed set of graph spectral bases. When the underlying true signals and complex noise patterns are severely aliased within this standard spectral domain, merely allocating localized weights over fixed basis vectors is fundamentally insufficient. The GFT lacks the essential degrees of freedom required to proactively decouple these entangled frequency components, ultimately limiting the denoising potential of current node-oriented methods in heavily corrupted scenarios.

To overcome the spectral rigidity of the standard GFT, researchers have recently explored various fractional-domain graph transforms, such as the graph fractional Fourier transform (GFRFT) [18]–[22], the multiple-parameter GFRFT (MPGFRFT) [23], and

the graph linear canonical transform (GLCT) [24]–[26]. These transforms break the fixed-basis limitation by introducing crucial extra degrees of freedom through tunable fractional parameters, enabling proactive spectral modulation to separate entangled signal and noise components that are otherwise inseparable in the standard GFT domain. By mapping graph signals into optimal intermediate transform spaces, fractional-domain filtering has demonstrated remarkable empirical success across a wide range of complex scenarios, including sensor network denoising, image reconstruction, and biological data analysis [27]–[33]. However, despite their spectral superiority, most existing fractional-domain filters are strictly designed as globally shared fractional filters, meaning they rigidly apply the same transform orders and spectral coefficients to every vertex across the graph. This global-sharing paradigm prevents these transforms from effectively accommodating the spatial irregularity and structural heterogeneity of complex networks. Such a fundamental limitation naturally raises a compelling question: how can we systematically integrate fractional transforms with node-oriented mechanisms to achieve both spatial adaptability and spectral flexibility?

Motivated by this fundamental question, this paper proposes a unified node-oriented fractional filtering (NOFF) framework, which systematically integrates the localized spatial adaptability of node-oriented filtering with the superior spectral flexibility of fractional-domain transforms. As conceptually illustrated in Fig. 1, the proposed NOFF architecture elegantly overcomes the dual limitations of existing methods, establishing a comprehensive paradigm that achieves both properties simultaneously. By generalizing node-wise spectral modulation from the rigid GFT domain to a wide range of fractional domains, including GFRFT, MPGFRFT, and GLCT, the NOFF framework allows each vertex to adaptively learn its own personalized filtering response within an optimal intermediate transform space. However, a straightforward implementation of the NOFF framework on large-scale graphs encounters a significant hurdle. Assigning unconstrained filters to all N vertices results in a prohibitive parameter space of N^2 . This immense parameterization not only leads to catastrophic memory consumption but also causes the model to memorize random graph noise rather than learning robust, physically meaningful filtering patterns, thereby severely compromising its generalization capability.

To mitigate these severe challenges on large-scale graphs with massive vertices, this paper introduces a low-rank node-oriented fractional filtering (LRNOFF) architecture. Rather than learning unconstrained dense filters, LRNOFF imposes a structural low-rank bottleneck on the ideal localized filter matrix. Crucially, this structural constraint inherently acts as an implicit regularizer during the end-to-end training process. By deliberately restricting the hypothesis space, it effectively prevents the model from memorizing high-frequency random noise, forcing the network to capture only the most essential and robust spectral filtering patterns. Ultimately, this synergistic design establishes a unified fractional filtering framework that seamlessly bridges the theoretical optimality of node-oriented spectral modulation with the robust regularization required for complex graph signal processing. The main contributions of this paper are summarized as follows:

- **NOFF framework:** We propose the NOFF framework, which introduces localized spatial adaptability into fractional-domain transforms (GFRFT, MPGFRFTs and GLCTs). This fundamentally overcomes both the spectral rigidity of standard node-oriented methods and the spatial limitations of globally

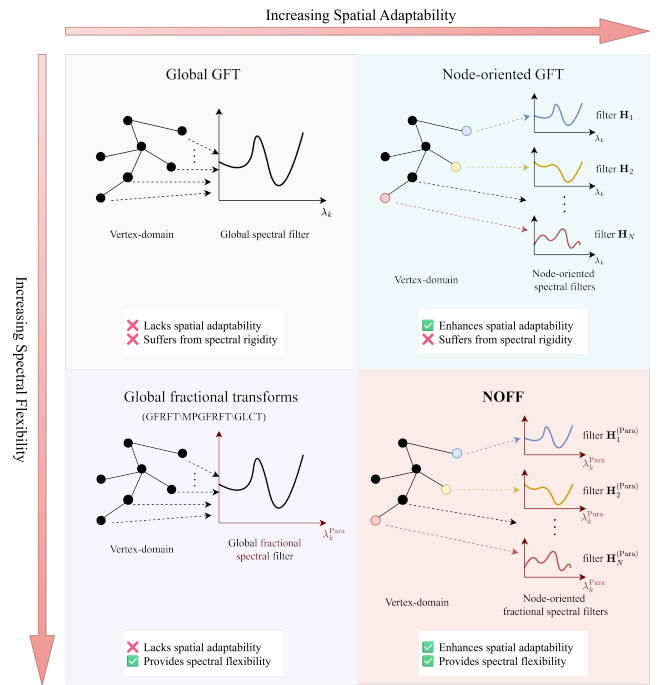


Fig. 1: Conceptual comparison of different graph spectral filtering paradigms.

shared fractional filters.

- **LRNOFF framework and implicit regularization:** We introduce the LRNOFF architecture by factorizing the ideal unconstrained filter matrix into a low-rank structure. We illustrate that this constraint naturally serves as an implicit regularizer, which drastically reduces the parameter space and prevents noise memorization.
- **Scalable LRNOFF-Fast implementation:** To facilitate practical deployment on massive real-world networks, we develop a scalable computational approach termed LRNOFF-Fast.
- **State-of-the-art denoising performance:** Experiments on real-world datasets demonstrate that our proposed framework consistently achieves state-of-the-art performance. The results explicitly validate the superiority of node-oriented mechanisms over globally shared filtering, and fractional-domain transforms over the standard GFT, while significantly outperforming advanced graph neural network (GNN) baselines.

The remainder of this paper is organized as follows. Section II introduces the essential preliminary concepts and notations. Section III presents the theoretical formulation of the proposed NOFF framework. Section IV introduces the scalable LRNOFF architecture, detailing its mathematical formulation and efficient computational strategy. Section V provides a comprehensive numerical evaluation of the proposed frameworks on both small-scale and large-scale graph datasets. Finally, Section VI concludes this paper. The comprehensive flowchart of the proposed NOFF and LRNOFF architectures is illustrated in Fig. 2. All the technical proofs of our theoretical results are relegated to the Appendix parts.

II. PRELIMINARIES

In this section, we briefly introduce some basic concepts of GSP and several fractional-domain transforms.

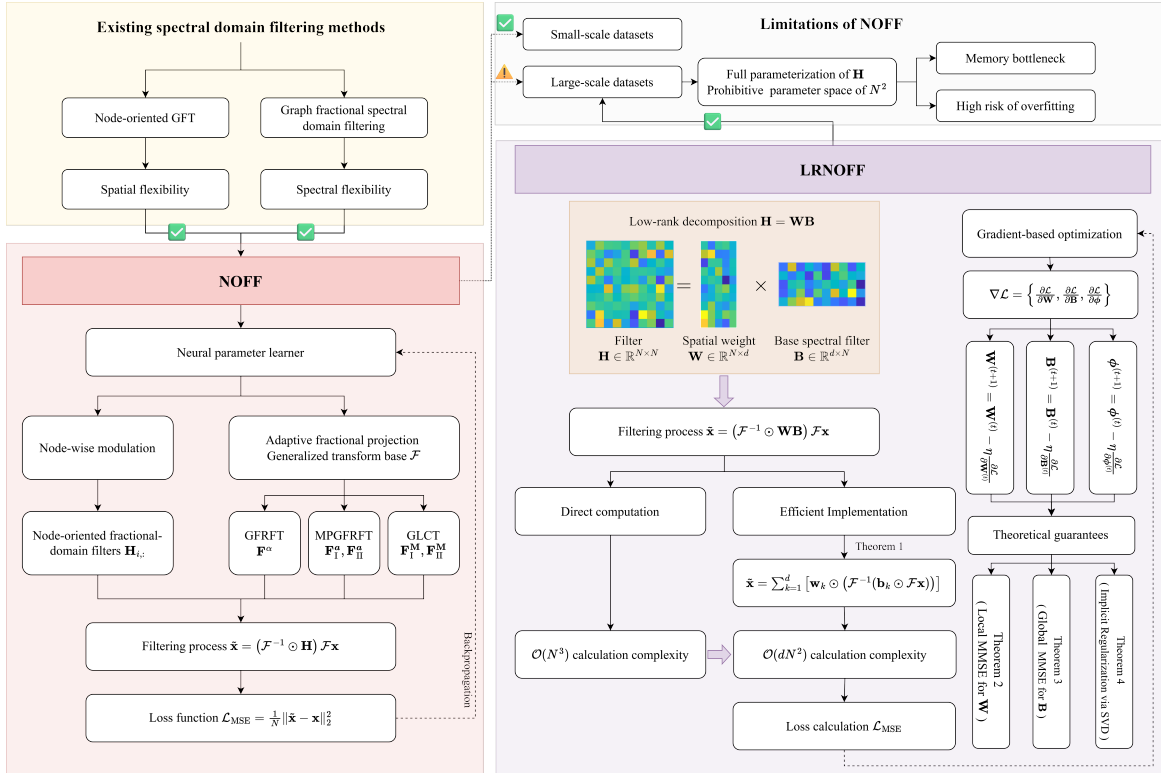


Fig. 2: The overall technical architecture of the proposed NOFF and its scalable LFNNOFF.

A. Graph signals and GFT

Consider an undirected weighted graph $\mathcal{G} = (\mathcal{V}, \mathcal{E}, \mathbf{W})$, where \mathcal{V} is the set of N vertices, \mathcal{E} is the set of edges, and $\mathbf{W} \in \mathbb{R}^{N \times N}$ is the weighted adjacency matrix. The degree matrix is $\mathbf{D} = \text{diag}(d_1, d_2, \dots, d_N)$ with $d_i = \sum_{j=1}^N W_{ij}$, and the Laplacian matrix is given by $\mathbf{L} = \mathbf{D} - \mathbf{W}$. A graph signal is defined as a vector $\mathbf{x} = [x_1, x_2, \dots, x_N]^T \in \mathbb{R}^N$.

Let \mathbf{S} denote a graph shift operator (GSO) (e.g., the adjacency matrix \mathbf{W} or the Laplacian matrix \mathbf{L}). In this paper, we assume that \mathbf{S} is a real symmetric matrix, which ensures it can be orthogonally diagonalized as $\mathbf{S} = \mathbf{V}\mathbf{\Lambda}\mathbf{V}^H$, where \mathbf{V} consists of the eigenvectors and $\mathbf{\Lambda} = \text{diag}(\lambda_0, \lambda_1, \dots, \lambda_{N-1})$ is the diagonal matrix of eigenvalues. The GFT of signal \mathbf{x} is defined as

$$\hat{\mathbf{x}} = \mathbf{F}\mathbf{x}, \quad (1)$$

where $\mathbf{F} = \mathbf{V}^H$ is the GFT matrix.

B. Fractional-domain graph transforms

To break through the limitation of the standard GFT, various fractional-domain transforms have been developed by generalizing the graph spectral domain.

By introducing a fractional order parameter $\alpha \in \mathbb{R}$ to provide a flexible intermediate domain between the vertex and spectral representations, the GFRFT is proposed.

Definition 1 (GFRFT): Given a fractional order parameter $\alpha \in \mathbb{R}$, the GFRFT matrix \mathbf{F}^α is defined as the fractional power of the standard GFT matrix [34]

$$\mathbf{F}^\alpha = \mathbf{V}\mathbf{\Lambda}^\alpha\mathbf{V}^H, \quad (2)$$

where $\mathbf{\Lambda}^\alpha = \text{diag}(\lambda_0^\alpha, \lambda_1^\alpha, \dots, \lambda_{N-1}^\alpha)$. For a graph signal \mathbf{x} , its α -th order GFRFT is given by

$$\hat{\mathbf{x}}_\alpha = \mathbf{F}^\alpha \mathbf{x}. \quad (3)$$

Furthermore, by assigning independent fractional orders to different spectral components, the MPGFRFT is proposed in our previous work [23]. This multiple-parameter mechanism provides higher degrees of freedom, inherently enabling proactive and fine-grained spectral modulation for complex graph signals. The MPGFRFT is defined in two forms.

Definition 2 (MPGFRFT-I): Given an order vector $\mathbf{a} = (a_0, a_1, \dots, a_{N-1})$, the MPGFRFT-I of signal \mathbf{x} is defined as

$$\hat{\mathbf{x}}_a^I = \mathbf{F}_I^{\mathbf{a}} \mathbf{x}, \quad (4)$$

where the MPGFRFT-I matrix $\mathbf{F}_I^{\mathbf{a}}$ is given by

$$\mathbf{F}_I^{\mathbf{a}} = \mathbf{V}\mathbf{\Lambda}_F^{\mathbf{a}}\mathbf{V}^{-1}, \quad (5)$$

with $\mathbf{\Lambda}_F^{\mathbf{a}} \triangleq \text{diag}(\lambda_0^{a_0}, \lambda_1^{a_1}, \dots, \lambda_{N-1}^{a_{N-1}})$.

Definition 3 (MPGFRFT-II): Given an order vector $\mathbf{a} = (a_0, a_1, \dots, a_{N-1})$, the MPGFRFT-II of signal \mathbf{x} with respect to the order vector \mathbf{a} is defined as

$$\hat{\mathbf{x}}_a^{II} = \mathbf{F}_{II}^{\mathbf{a}} \mathbf{x}, \quad (6)$$

where the MPGFRFT-II matrix $\mathbf{F}_{II}^{\mathbf{a}}$ is expressed as

$$\mathbf{F}_{II}^{\mathbf{a}} = \sum_{n=0}^{N-1} C_{n, a_n}^{II} \mathbf{F}^n, \quad (7)$$

with the coefficients

$$C_{n, a_n}^{II} = \sum_{j=0}^{N-1} p_{n+1, j+1} \lambda_j^{a_n}. \quad (8)$$

The constant matrix $\mathbf{P} = (p_{ij})$ is

$$\mathbf{P} = (p_{ij}) \triangleq \begin{pmatrix} 1 & \lambda_0 & \dots & \lambda_0^{N-1} \\ 1 & \lambda_1 & \dots & \lambda_1^{N-1} \\ \vdots & \vdots & \ddots & \vdots \\ 1 & \lambda_{N-1} & \dots & \lambda_{N-1}^{N-1} \end{pmatrix}^{-1}. \quad (9)$$

In addition to the aforementioned transforms, the GLCT introduces an alternative parameterized framework. For a given parameter matrix $\mathbf{M} = (a, b; c, d)$ satisfying $ad - bc = 1$, the continuous parameters are mapped as $\xi = \frac{ac+bd}{a^2+b^2}$, $\sigma = \sqrt{a^2+b^2}$, and $\alpha = \frac{2}{\pi} \cos^{-1} \left(\frac{a}{\sigma} \right) = \frac{2}{\pi} \sin^{-1} \left(\frac{b}{\sigma} \right)$. Based on centered discrete Hermite-Gaussian functions (CDDHFs), the GLCT is defined under different GSOs.

Definition 4 (Lap-CDDHFs-GLCT): Using the Laplacian matrix \mathbf{L} , the Lap-CDDHFs-GLCT of signal \mathbf{x} is defined as

$$\hat{\mathbf{x}}_{\mathbf{M}}^{\text{I}} = \mathbf{F}_{\text{I}}^{\text{M}} \mathbf{x}, \quad (10)$$

and the transformation matrix $\mathbf{F}_{\text{I}}^{\text{M}}$ is given by

$$\mathbf{F}_{\text{I}}^{\text{M}} = \mathcal{C}\mathcal{M}_{\text{L}}^{\xi} \mathbf{S}_{\text{L}} \mathbf{P}_{\text{L}} \mathbf{J}_{\text{L}}^{\alpha} \mathbf{P}_{\text{L}}^{-1}, \quad (11)$$

where \mathbf{P}_{L} is the eigenvector matrix of \mathbf{L} , and \mathbf{J}_{L} is the diagonal eigenvalue matrix. The operator \mathbf{S}_{L} is the Laplacian-based graph scaling matrix, constructed as

$$\mathbf{S}_{\text{L}} = \text{diag}([\sigma^{-\varepsilon r_0}, \sigma^{-\varepsilon r_1}, \dots, \sigma^{-\varepsilon r_{N-1}}]), \quad (12)$$

where r_l ($l = 0, \dots, N-1$) represents the eigenvalues corresponding to the eigenvector matrix \mathbf{P}_{L} , and ε represents the rate of scale change. The operator $\mathcal{C}\mathcal{M}_{\text{L}}^{\xi}$ represents the Laplacian-based graph chirp multiplication matrix

$$\mathcal{C}\mathcal{M}_{\text{L}}^{\xi} = \text{diag}(\mathbf{P}_{\text{L}} \hat{\mathbf{s}}_{\xi}), \quad (13)$$

where $\hat{\mathbf{s}}_{\xi}$ is the spectral chirp signal vector whose k -th element is given by $\hat{s}_{\xi}(k) = e^{-i \frac{\lambda_k^2}{\xi}}$.

Definition 5 (wAdj-CDDHFs-GLCT): Using the weighted adjacency matrix \mathbf{W} , the wAdj-CDDHFs-GLCT of signal \mathbf{x} is defined as

$$\hat{\mathbf{x}}_{\mathbf{M}}^{\text{II}} = \mathbf{F}_{\text{II}}^{\text{M}} \mathbf{x}, \quad (14)$$

and the transformation matrix $\mathbf{F}_{\text{II}}^{\text{M}}$ is given by

$$\mathbf{F}_{\text{II}}^{\text{M}} = \mathbf{J}_{\text{W}}^{\xi} \mathbf{P}_{\sigma} \mathbf{J}_{\text{W}}^{\alpha} \mathbf{P}_{\text{W}}^{-1}, \quad (15)$$

where \mathbf{P}_{W} is the eigenvector matrix of \mathbf{W} , \mathbf{J}_{W} denotes the corresponding eigenvalue matrix, and \mathbf{P}_{σ} is the eigenvector matrix of the scaled adjacency matrix $\frac{1}{\sigma} \mathbf{W}$.

For simplicity of presentation in the subsequent sections, the term ‘‘CDDHFs’’ will be omitted, and these two transforms will be abbreviated as Lap-GLCT and wAdj-GLCT, respectively.

III. NODE-ORIENTED FRACTIONAL-DOMAIN FILTERING

In GSP, graph filters are typically designed as global operators shared across the entire graph. Given an observed signal \mathbf{x} , the global filtering process in the standard graph spectral domain can be expressed as

$$\mathbf{y} = \mathbf{V} \mathbf{H}_{\text{diag}} \mathbf{V}^{\text{H}} \mathbf{x}, \quad (16)$$

where $\mathbf{H}_{\text{diag}} = \text{diag}(h_1, h_2, \dots, h_N)$ is the filter.

However, the globally shared filter fails to adapt to the spatial heterophily of real-world graph data. To address this, Zheng *et al.* [17] proposed a node-oriented filtering mechanism that assigns independent spectral filtering weights to each vertex, significantly enhancing spatial adaptability. Although effective, this method is strictly confined to the standard graph spectral domain and lacks the capability for proactive spectral modulation. To simultaneously overcome spatial heterophily and spectral rigidity, we propose a node-oriented fractional-domain graph filtering method. By integrating spatial adaptation into the generalized fractional-domain systems defined in Section II, our filter endows each vertex with exclusive spectral coefficients and leverages fractional degrees of freedom to perform proactive and fine-grained signal extraction.

A. Node-oriented fractional filtering

For notational convenience, we uniformly use \mathcal{F} and \mathcal{F}^{-1} to denote any forward and inverse fractional-domain transform matrices, respectively. Depending on the specific generalized fractional-domain systems defined in Section II, \mathcal{F} can represent any of the five previously introduced matrix forms, i.e. $\{\mathbf{F}^{\alpha}, \mathbf{F}_{\text{I}}^{\alpha}, \mathbf{F}_{\text{II}}^{\alpha}, \mathbf{F}_{\text{I}}^{\text{M}}, \mathbf{F}_{\text{II}}^{\text{M}}\}$.

In practical applications, the pure graph signal $\mathbf{x} \in \mathbb{R}^N$ is typically corrupted by noise. Let $\mathbf{y} \in \mathbb{R}^N$ denote the observed noisy signal, modeled as $\mathbf{y} = \mathbf{x} + \mathbf{n}$, where $\mathbf{n} \in \mathbb{R}^N$ represents the additive noise. The goal of graph filtering is to effectively recover the original signal \mathbf{x} from the noisy observation \mathbf{y} .

Instead of utilizing a single shared spectral response vector for the entire graph, we assign a customized filter to each vertex. To this end, we define a learnable dense coefficient matrix $\mathbf{H} \in \mathbb{R}^{N \times N}$, where the i -th row $\mathbf{H}_{i,:}$ encapsulates the exclusive spectral coefficients for the i -th node. Consequently, the filtering output for a specific node i is obtained by applying its personalized spectral response to the transformed graph signal and extracting the i -th observation. Mathematically, this process can be expressed as

$$\begin{aligned} \tilde{x}_i &= \delta_i^{\top} \mathcal{F}^{-1} \text{diag}(\mathbf{H}_{i,:}) \mathcal{F} \mathbf{x} \\ &= \sum_{k=1}^N \mathcal{F}_{i,k}^{-1} H_{i,k} (\mathcal{F} \mathbf{x})_k, \end{aligned} \quad (17)$$

where $\delta_i \in \mathbb{R}^N$ denotes the i -th standard basis column vector.

By generalizing this node-wise operation to the entire graph, the overall filtered signal $\tilde{\mathbf{y}}$ can be elegantly formulated in a compact matrix form using the Hadamard product \odot as

$$\tilde{\mathbf{x}} = (\mathcal{F}^{-1} \odot \mathbf{H}) \mathcal{F} \mathbf{x}. \quad (18)$$

Remark 1: When the \mathcal{F} reduces to the GFT matrix, the proposed mechanism strictly reduces to the node-oriented spectral filtering method presented in [17]. When $\mathbf{H}_{1,:} = \mathbf{H}_{2,:} = \dots = \mathbf{H}_{N,:}$, the proposed mechanism naturally degrades to the traditional global fractional-domain graph filtering [20].

To optimize the filter coefficient matrix \mathbf{H} , we employ the mean squared error (MSE) as the objective function

$$\mathcal{L}_{\text{MSE}} = \frac{1}{N} \|\tilde{\mathbf{x}} - \mathbf{x}\|_2^2, \quad (19)$$

where $\|\cdot\|_2$ denotes the ℓ_2 -norm.

Furthermore, the signal-to-noise ratio (SNR) provides a standard measure of the reconstruction fidelity and is formulated as

$$\text{SNR} = 20 \log_{10} \frac{\|\mathbf{x}\|_2}{\|\tilde{\mathbf{x}} - \mathbf{x}\|_2}. \quad (20)$$

B. Neural network architecture implementation

The proposed NOFF mechanism is implemented as an end-to-end trainable network composed of stacked node-oriented fractional filter layers.

At the l -th layer, let $\mathbf{H}^{(l)} \in \mathbb{R}^{N \times N}$ denote the learnable coefficient matrix, where the i -th row $\mathbf{H}_{i,:}^{(l)}$ specifies the vertex-dependent spectral response of node i . Meanwhile, the forward and inverse generalized fractional-domain transforms are parameterized by layer-specific learnable variables, denoted by $\mathcal{F}^{(l)}$ and $(\mathcal{F}^{(l)})^{-1}$, respectively. Their exact forms depend on the selected generalized fractional-domain system in Section II. Let $\mathbf{x}^{(0)} = \mathbf{y}$ denote the noisy input. Then the output of the l -th filter layer is given by

$$\mathbf{z}^{(l+1)} = \left((\mathcal{F}^{(l)})^{-1} \odot \mathbf{H}^{(l)} \right) \mathcal{F}^{(l)} \mathbf{x}^{(l)}. \quad (21)$$

TABLE I: Summary of implementations in the NOFF framework

Method	Layer formulation $\mathbf{z}^{(l+1)}$	Filtering domain	Learnable parameters	Spectral Advantage & Role
NOFF-GFT	$(\mathbf{F}^{-1} \odot \mathbf{H}^{(l)}) \mathbf{F} \mathbf{x}^{(l)}$	GFT	\mathbf{H}	Rigid spectral basis. Serves as a baseline, but lacks flexibility to decouple complex aliased noise.
NOFF-GFRFT	$\left(((\mathbf{F}^\alpha)^{-1})^{(l)} \odot \mathbf{H}^{(l)} \right) (\mathbf{F}^\alpha)^{(l)} \mathbf{x}^{(l)}$	GFRFT	\mathbf{H}, α	Global fractional power. Effective for separating globally uniform noise via non-linear spectral scaling.
NOFF-MPGFRFT-I	$\left(((\mathbf{F}_I^\alpha)^{-1})^{(l)} \odot \mathbf{H}^{(l)} \right) (\mathbf{F}_I^\alpha)^{(l)} \mathbf{x}^{(l)}$	MPGFRFT-I	\mathbf{H}, α	Independent fractional power per spectral component. Essential for decoupling multi-scale heterogeneous patterns.
NOFF-MPGFRFT-II	$\left(((\mathbf{F}_{II}^\alpha)^{-1})^{(l)} \odot \mathbf{H}^{(l)} \right) (\mathbf{F}_{II}^\alpha)^{(l)} \mathbf{x}^{(l)}$	MPGFRFT-II	\mathbf{H}, α	Fine-grained modulation via matrix polynomials. Maximizes adaptive capacity to resolve highly localized anomalies.
NOFF-Lap-GLCT	$\left(((\mathbf{F}_I^M)^{-1})^{(l)} \odot \mathbf{H}^{(l)} \right) (\mathbf{F}_I^M)^{(l)} \mathbf{x}^{(l)}$	Lap-GLCT	\mathbf{H}, M	Laplacian-based affine parameterization. Specifically targets and compensates for topological spectral shifts.
NOFF-wAdj-GLCT	$\left(((\mathbf{F}_{II}^M)^{-1})^{(l)} \odot \mathbf{H}^{(l)} \right) (\mathbf{F}_{II}^M)^{(l)} \mathbf{x}^{(l)}$	wAdj-GLCT	\mathbf{H}, M	Adjacency-based affine transformation. Uniquely suited to capture asymmetric signal propagation and complex structural dynamics.

To improve representation capability and stabilize training, residual connections are introduced between consecutive layers. In this work, a three-layer architecture is adopted. For the first two layers, the hidden representations are updated by

$$\mathbf{x}^{(l+1)} = \text{ReLU}\left(\Re(\mathbf{x}^{(l)} + \mathbf{z}^{(l+1)})\right), \quad l \in \{0, 1\}, \quad (22)$$

where $\Re(\cdot)$ denotes the real-part operator, and $\text{ReLU}(\cdot)$ denotes the rectified linear unit activation. In the last layer, the activation function is omitted to avoid truncating negative signal values, and the final reconstructed signal is obtained as

$$\tilde{\mathbf{x}} = \mathbf{x}^{(2)} + \mathbf{z}^{(3)}. \quad (23)$$

It is crucial to emphasize that the proposed NOFF is designed as a highly flexible and unified framework rather than being restricted to a single specific transform. We first clarify the terminology used throughout this paper to distinguish between different filtering paradigms. For any specific fractional transform, we evaluate both its global and node-oriented implementations. In the global fractional filtering (GFF) variants, abbreviated as GFF-[Transform], a single identical spectral response is shared across all vertices. In contrast, our proposed node-oriented fractional filtering variants, denoted as NOFF-[Transform], assign customized spectral responses to individual nodes. As systematically compared in Table I, various fractional domains can be seamlessly instantiated within the proposed NOFF framework to address distinct physical challenges.

The overall training and inference procedure of the proposed network is summarized in Algorithm 1. This localized architecture empowers the model to capture complex topological variations.

However, it is important to acknowledge the inherent limitations of this ideal formulation. While the unconstrained NOFF theoretically provides exceptional spatial-spectral adaptability, its direct application to large-scale graphs encounters a severe curse of dimensionality. For a graph with N vertices, the unconstrained filter matrix \mathbf{H} requires N^2 independent spectral parameters per layer. When N becomes massive, this excessively vast parameter space not only incurs prohibitive memory and computational costs but also introduces a severe risk of overfitting, leading the model to memorize random graph noise. Therefore, it is imperative to

Algorithm 1 Training and inference of the proposed NOFF network

Require: Training set \mathcal{D}_{tr} , validation set \mathcal{D}_{val} , test set \mathcal{D}_{te} , GSO \mathbf{S} , maximum epoch E , learning rate η
Ensure: Learned filter matrices $\{\mathbf{H}^{(l)}\}_{l=0}^2$, learned layer-specific transform parameters, and the final filtered signal $\tilde{\mathbf{x}}$

- 1: **Initialization:** Compute the transform basis from \mathbf{S} and initialize filter matrices $\mathbf{H}_{l=0}^{(l)}$ and layer-specific transform parameters
- 2: **for** each epoch $e = 1, 2, \dots, E$ **do**
- 3: **for** each training sample pair $(\mathbf{y}, \mathbf{x}) \in \mathcal{D}_{\text{tr}}$ **do**
- 4: Set $\mathbf{x}^{(0)} \leftarrow \mathbf{y}$
- 5: **for** $l = 0, 1, 2$ **do**
- 6: Compute $\mathbf{z}^{(l+1)} = ((\mathcal{F}^{(l)})^{-1} \odot \mathbf{H}^{(l)}) \mathcal{F}^{(l)} \mathbf{x}^{(l)}$
- 7: **if** $l < 2$ **then**
- 8: Update $\mathbf{x}^{(l+1)} \leftarrow \text{ReLU}(\Re(\mathbf{x}^{(l)} + \mathbf{z}^{(l+1)}))$
- 9: **end if**
- 10: **end for**
- 11: Obtain $\tilde{\mathbf{x}} \leftarrow \mathbf{x}^{(2)} + \mathbf{z}^{(3)}$
- 12: **Loss Computation & Optimization:** Compute $\mathcal{L}_{\text{MSE}} = \|\tilde{\mathbf{x}} - \mathbf{x}\|_2^2$ and update $\{\mathbf{H}^{(l)}, \mathcal{F}^{(l)}\}_{l=0}^2$ using Adam
- 13: **end for**
- 14: After each epoch, evaluate the validation loss on \mathcal{D}_{val}
- 15: Update the learning rate scheduler and early-stopping state according to the validation loss
- 16: **end for**
- 17: Load the best saved network parameters and reconstruct the signals in \mathcal{D}_{te}
- 18: Compute the test SNR and report

structurally regularize the parameter space to handle large-scale networks effectively. We will address this critical computational challenge in the following section.

IV. SCALABLE NODE-ORIENTED FRACTIONAL FILTERING VIA LOW-RANK APPROXIMATION

To overcome the curse of dimensionality and the risk of overfitting inherent in the unconstrained NOFF model, this section proposes a scalable LRNOFF architecture. By imposing a structural

bottleneck, we drastically reduce the parameter space while preserving the adaptability.

A. Low-rank formulation and efficient computation

To mitigate this scalability bottleneck, we introduce a low-rank approximation algorithm for the dense coefficient matrix \mathbf{H} . Specifically, we constrain \mathbf{H} by decomposing it into the product of two low-rank sub-matrices:

$$\mathbf{H} = \mathbf{W}\mathbf{B}, \quad (24)$$

where the spatial weight matrix $\mathbf{W} \in \mathbb{R}^{N \times d}$ and the base spectral filter matrix $\mathbf{B} \in \mathbb{R}^{d \times N}$, with the rank satisfying $d \ll N$. Consequently, the filtering coefficient for the i -th node and j -th spectral component is given by $H_{i,j} = \sum_{k=1}^d W_{i,k} B_{k,j}$.

Without the low-rank structure, computing the naive node-oriented filtering directly from its definition requires executing the spectral response mapping for each vertex independently, which yields a complexity of $\mathcal{O}(N^3)$. Such an extensive computational burden is impractical for large-scale graph analysis. However, by substituting the low-rank constraint into the filtering equation, the overall computation can be elegantly decoupled and accelerated. We formalize this efficient computational process in the following theorem.

Theorem 1: Given the forward and inverse fractional-domain transform matrices \mathcal{F} and \mathcal{F}^{-1} , the input signal \mathbf{x} , and the low-rank filter decomposition $\mathbf{H} = \mathbf{W}\mathbf{B}$ with rank d , the filtered output $\tilde{\mathbf{x}} = (\mathcal{F}^{-1} \odot \mathbf{H}) \mathcal{F}\mathbf{x}$ can be equivalently computed as

$$\tilde{\mathbf{x}} = \sum_{k=1}^d [\mathbf{w}_k \odot (\mathcal{F}^{-1}(\mathbf{b}_k \odot \mathcal{F}\mathbf{x}))], \quad (25)$$

where $\mathbf{w}_k = \mathbf{W}_{:,k} \in \mathbb{C}^N$ represents the k -th column of \mathbf{W} , and $\mathbf{b}_k = (\mathbf{B}_{k,:})^\top \in \mathbb{C}^N$ represents the transpose of the k -th row of \mathbf{B} .

Proof: See Appendix A.

Remark 2 (Complexity analysis): Before evaluating the computational efficiency, it is crucial to clarify that the construction of bases \mathcal{F} and \mathcal{F}^{-1} is assumed to be pre-computed as a standard pre-processing step in GSP. We focus strictly on the matrix calculation complexity of the filtering operation itself.

- **GFF:** Since all nodes share a single spectral response vector, the operation involves one forward transform, one diagonal multiplication, and one inverse transform, resulting in a matrix calculation complexity of $\mathcal{O}(N^2)$.
- **Unconstrained NOFF:** Without the low-rank constraint, each node independently learns its own response. The unconstrained dense matrix operations yield a complexity of $\mathcal{O}(N^3)$.
- **Low-rank NOFF via direct computation (LRNOFF-Direct):** Even if the low-rank constraint $\mathbf{H} = \mathbf{W}\mathbf{B}$ is applied, computing the filter directly without the summation rearrangement of Theorem 1 requires evaluating the coupled dense matrix operations. This still incurs a complexity of $\mathcal{O}(N^3)$, which fails to resolve the computational bottleneck.
- **Low-rank NOFF via Theorem 1 (LRNOFF-Fast):** As demonstrated in Theorem 1, the computation is decoupled into d parallel fractional transform operations. This allows the matrix calculation complexity to drop significantly to $\mathcal{O}(dN^2)$.

Remark 3 (Physical interpretation): From a physical perspective, the decomposition $\mathbf{H} = \mathbf{W}\mathbf{B}$ provides a meaningful interpretation

of the filtering process. The matrix \mathbf{B} acts as a *global dictionary* that learns d fundamental fractional-spectral filtering patterns across the entire graph. Meanwhile, \mathbf{W} functions as an *adaptive allocator* that assigns localized weights for each vertex, smoothly blending these base patterns to accommodate the distinct topological neighborhood of each node.

To systematically summarize the architectural evolution and the aforementioned advantages, Table II provides a comprehensive comparison of different filtering paradigms. It is evident that the proposed LRNOFF-Fast perfectly balances localized spatial adaptability, implicit regularization, and strict computational efficiency, rendering it highly scalable for large-scale graphs.

The closed-form optimal solution for GFF has been rigorously established by Ozturk et al. [20]. By constraining the fractional filter to a global diagonal matrix parameterized by a single response vector $\mathbf{h}_{opt} \in \mathbb{C}^{N \times 1}$, the optimal global filter coefficients are obtained by solving the linear system $\mathbf{T}\mathbf{h}_{opt} = \mathbf{q}$. However, achieving optimal node-oriented filtering requires removing this rigid global sharing constraint and assigning an independent filtering response to each vertex. The ideal unconstrained local filter vector for the i -th vertex, denoted as $\mathbf{h}_{opt}^{(i)} \in \mathbb{C}^{N \times 1}$, can be derived by individually minimizing its localized reconstruction MSE.

By vertically concatenating these optimal unconstrained responses of all N vertices, we can explicitly construct the complete, ideal node-oriented fractional filter matrix

$$\mathbf{H}_{opt} = [\mathbf{h}_{opt}^{(1)}, \mathbf{h}_{opt}^{(2)}, \dots, \mathbf{h}_{opt}^{(N)}]^\top \in \mathbb{C}^{N \times N}. \quad (26)$$

B. Theoretical analysis and optimization of the LRNOFF-Fast

The proposed LRNOFF-Fast is implemented as an end-to-end trainable framework, sharing a similar architectural philosophy with the NOFF introduced in Section III. Let \mathcal{L} denote the MSE loss function and η denote the learning rate. During the backpropagation process, the network parameters are updated iteratively via gradient descent. The complete gradient of the loss function with respect to all learnable parameters is defined as

$$\nabla \mathcal{L} = \left\{ \frac{\partial \mathcal{L}}{\partial \mathbf{W}}, \frac{\partial \mathcal{L}}{\partial \mathbf{B}}, \frac{\partial \mathcal{L}}{\partial \phi} \right\}. \quad (27)$$

At the t -th iteration, the spatial weight matrix \mathbf{W} , the base spectral filter matrix \mathbf{B} , and the fractional-domain parameter ϕ (e.g., the fractional order α in GFRFT, the fractional order vector \mathbf{a} in MPGRFT, or the matrix \mathbf{M} in GLCT) are updated by

$$\mathbf{W}^{(t+1)} = \mathbf{W}^{(t)} - \eta \frac{\partial \mathcal{L}}{\partial \mathbf{W}^{(t)}}, \quad (28)$$

$$\mathbf{B}^{(t+1)} = \mathbf{B}^{(t)} - \eta \frac{\partial \mathcal{L}}{\partial \mathbf{B}^{(t)}}, \quad (29)$$

$$\phi^{(t+1)} = \phi^{(t)} - \eta \frac{\partial \mathcal{L}}{\partial \phi^{(t)}}. \quad (30)$$

For the spatial and spectral filter components, the gradients drive the model to learn the optimal localized blending and global base patterns, respectively. Since the generalized fractional transforms are fully differentiable with respect to their defining variables, the optimization of the fractional parameter ϕ is directly handled through standard automatic differentiation to dynamically search for the optimal transform domain. By the fundamental definition of partial differentiation, computing the gradient for one specific parameter matrix inherently treats the remaining variables as constants. To provide a rigorous theoretical guarantee

TABLE II: Comprehensive comparison of theoretical attributes among various filtering paradigms

Method	Spatial adaptability	Implicit regularization	Filter parameters	Computational complexity	Large-scale feasibility
GFF	Global	×	$\mathcal{O}(N)$	$\mathcal{O}(N^2)$	✓
Unconstrained NOFF	Node-oriented	×	$\mathcal{O}(N^2)$	$\mathcal{O}(N^3)$	×
LRNOFF-Direct	Node-oriented	✓(Low-rank)	$\mathcal{O}(dN)$	$\mathcal{O}(N^3)$	✓
LRNOFF-Fast	Node-oriented	✓(Low-rank)	$\mathcal{O}(dN)$	$\mathcal{O}(dN^2)$	✓

for this gradient-based learning process, the following two theorems demonstrate that under such conditional fixation, the separate optimizations of \mathbf{W} and \mathbf{B} correspond directly to deriving exact, closed-form minimum MSE (MMSE) solutions.

Theorem 2: Assume the base spectral filter matrix \mathbf{B} is fixed, and let \mathbf{u}_k denote the k -th base filtered signal mapped to the vertex domain. For the i -th vertex, let $\mathbf{u}^{(i)} = [U_{i,1}, U_{i,2}, \dots, U_{i,d}]^\top$, and $\mathbf{w}^{(i)} = [W_{i,1}, W_{i,2}, \dots, W_{i,d}]^\top$. By minimizing the local MSE cost function $J(\mathbf{w}^{(i)}) = \mathbb{E}[|\tilde{x}_i - x_i|^2]$, the optimal spatial weight vector is derived as

$$\mathbf{w}_{opt}^{(i)} = (\mathbf{R}_U^{(i)})^{-1} \mathbf{r}_{Ux}^{(i)}, \quad \forall i \in \{1, 2, \dots, N\}, \quad (31)$$

where $\mathbf{R}_U^{(i)} = \mathbb{E}[(\mathbf{u}^{(i)})^* (\mathbf{u}^{(i)})^\top] \in \mathbb{C}^{d \times d}$ is the local auto-correlation matrix, and $\mathbf{r}_{Ux}^{(i)} = \mathbb{E}[(\mathbf{u}^{(i)})^* x_i] \in \mathbb{C}^{d \times 1}$ is the cross-correlation vector. The superscript $*$ denotes the complex conjugate.

Proof: See Appendix B.

Theorem 3: Assume the spatial weight matrix \mathbf{W} is fixed, and let $\Psi = \mathcal{F}^{-1} \text{diag}(\mathcal{F}\mathbf{y}) \in \mathbb{C}^{N \times N}$ be the combined transform matrix for the input signal \mathbf{y} . By vectorizing the base filter matrix as a global column vector $\mathbf{b} = [(\mathbf{b}^{(1)})^\top, (\mathbf{b}^{(2)})^\top, \dots, (\mathbf{b}^{(d)})^\top]^\top \in \mathbb{C}^{dN \times 1}$ where $\mathbf{b}^{(k)} = (\mathbf{B}_{k,:})^\top$, and defining a concatenated spatial-spectral feature row vector for node i as $\mathbf{v}^{(i)} = [W_{i,1}\Psi_{i,:}, \dots, W_{i,d}\Psi_{i,:}] \in \mathbb{C}^{1 \times dN}$, the optimal global base filter vector \mathbf{b} that minimizes the global MSE $J(\mathbf{b}) = \sum_{i=1}^N \mathbb{E}[|\mathbf{v}^{(i)}\mathbf{b} - x_i|^2]$ is given by

$$\mathbf{b}_{opt} = \mathbf{R}_V^{-1} \mathbf{r}_{Vx}, \quad (32)$$

where $\mathbf{R}_V = \sum_{i=1}^N \mathbb{E}[(\mathbf{v}^{(i)})^H \mathbf{v}^{(i)}] \in \mathbb{C}^{dN \times dN}$ is the global auto-correlation matrix, and $\mathbf{r}_{Vx} = \sum_{i=1}^N \mathbb{E}[(\mathbf{v}^{(i)})^H x_i] \in \mathbb{C}^{dN \times 1}$ is the global cross-correlation vector.

Proof: See Appendix C.

Remark 3 (Structural disparity in objective functions): It is crucial to note the fundamental discrepancy between the objective functions employed in Theorems 2 and 3. Since the spatial weight matrix \mathbf{W} assigns an independent vector to each specific node, its optimization can be mathematically decoupled into N independent local MMSE problems. In contrast, the base spectral filter matrix \mathbf{B} acts as a globally shared dictionary across the entire graph. Consequently, the parameters in \mathbf{B} cannot be decoupled node-by-node; their optimization must be formulated as a joint global MMSE problem that minimizes the aggregated reconstruction error over all vertices simultaneously.

Remark 4 (Theoretical guarantee for gradient-based learning): Theorems 2 and 3 provide a rigorous statistical signal processing foundation for the iterative gradient descent updates of the network. In practice, the model dynamically updates the parameters via partial derivatives (i.e., descending along $\frac{\partial \mathcal{L}}{\partial \mathbf{W}}$ and $\frac{\partial \mathcal{L}}{\partial \mathbf{B}}$) rather than directly calculating the computationally prohibitive matrix inversions required by the exact Wiener solutions. However, these theorems mathematically guarantee that the conditional loss landscape for each parameter block is strictly convex. Consequently, the partial gradients computed during backpropagation are theoretically

well-posed, stably guiding the optimization trajectory toward the exact closed-form MMSE optimums without the risk of gradient divergence.

To establish the structural validity of our proposed low-rank architecture, the following theorem demonstrates how this massive, parameter-heavy ideal filter matrix \mathbf{H}_{opt} can be optimally approximated.

Theorem 4: Assume the ideal unconstrained filter matrix \mathbf{H}_{opt} defined in Eq. (26) admits the singular value decomposition (SVD) $\mathbf{H}_{opt} = \mathbf{U}\Sigma\mathbf{V}^H$. Under the low-rank constraint $\text{rank}(\mathbf{H}) \leq d$, the global optimal matrix \mathbf{H}_d^* that minimizes the Frobenius norm approximation error $\|\mathbf{H}_{opt} - \mathbf{H}\|_F^2$ is exactly given by the truncated SVD

$$\mathbf{H}_d^* = \mathbf{U}_d \Sigma_d \mathbf{V}_d^H, \quad (33)$$

where $\mathbf{U}_d \in \mathbb{C}^{N \times d}$ and $\mathbf{V}_d \in \mathbb{C}^{N \times d}$ contain the first d left and right singular vectors, respectively, and $\Sigma_d \in \mathbb{R}^{d \times d}$ is the diagonal matrix of the d largest singular values. Furthermore, this optimal projection can be symmetrically factorized into a localized spatial weight matrix $\mathbf{W}_{opt} \in \mathbb{C}^{N \times d}$ and a global base spectral filter matrix $\mathbf{B}_{opt} \in \mathbb{C}^{d \times M}$, given by

$$\mathbf{W}_{opt} = \mathbf{U}_d \Sigma_d^{1/2}, \quad (34)$$

$$\mathbf{B}_{opt} = \Sigma_d^{1/2} \mathbf{V}_d^H. \quad (35)$$

Proof: See Appendix D.

Remark 5 (Bridging analytical SVD projection with implicit regularization): Theorem 4 mathematically justifies our decoupled $\mathbf{W}\mathbf{B}$ architecture. It proves that while the ideal unconstrained filter \mathbf{H}_{opt} requires a massive parameter space, its most essential and dominant spectral filtering properties can be optimally captured and bounded within a low-rank subspace governed by the principal singular values. In practical large-scale applications, rather than directly calculating the highly complex \mathbf{H}_{opt} , which would easily lead to severe overfitting on random noise, our proposed LRNOFF-Fast adopts this theoretically guaranteed $\mathbf{W}\mathbf{B}$ structure as a hypothesis space. By dynamically optimizing \mathbf{W} and \mathbf{B} via end-to-end MSE minimization, the low-rank constraint ($d \ll N$) acts as a powerful implicit regularizer. It strictly forces the network to learn the noise-free principal filter bases (analogous to \mathbf{B}_{opt}) and their spatial combinations (analogous to \mathbf{W}_{opt}), perfectly aligning the mathematical optimum with robust, data-driven empirical performance.

V. EXPERIMENTS

A. Experiments on small-scale graphs

Datasets and Graph Construction: To evaluate denoising performance on graph signals, we consider two representative real-world datasets, namely the Quality dataset ($N = 7$) [35] and the Exchange-rate dataset ($N = 8$) [36]. For each dataset, we use symmetric adjacency matrix $\mathbf{A}_{\text{sym}} = (\mathbf{A} + \mathbf{A}^\top)/2$ and the normalized symmetric graph Laplacian $\mathbf{L}_{\text{sym}} = \mathbf{I} - \mathbf{D}^{-1/2} \mathbf{A}_{\text{sym}} \mathbf{D}^{-1/2}$. The

TABLE III: Denoising performance comparison of GFF-based and NOFF-based methods on small-scale datasets.

Dataset	Quality				Exchange-rate			
	50	80	150	200	0.5	0.8	1	1.2
σ								
SNR	3.949	-0.133	-5.593	-8.092	4.209	0.126	-1.812	-3.395
GFF-GFRFT	10.230	8.094	5.471	4.841	11.973	8.581	7.599	7.428
NOFF-GFRFT	10.616	8.388	6.045	5.410	13.202	11.478	10.940	10.657
GFF-MPGFRFT-I	10.536	8.304	5.878	5.169	13.326	11.137	10.325	8.975
NOFF-MPGFRFT-I	10.604	8.346	5.930	5.388	13.804	11.864	11.420	10.991
GFF-MPGFRFT-II	10.421	7.879	5.492	4.605	10.168	11.351	10.869	8.936
NOFF-MPGFRFT-II	10.422	8.376	5.812	4.868	13.929	11.842	11.317	10.460
GFF-Lap-GLCT	10.272	8.184	5.870	4.688	11.855	8.672	7.585	7.786
NOFF-Lap-GLCT	10.471	8.272	5.933	5.428	13.187	11.455	10.878	10.683
GFF-wAdj-GLCT	10.488	8.117	5.394	4.613	13.321	9.832	9.733	9.275
NOFF-wAdj-GLCT	10.513	8.336	5.994	5.224	13.442	11.512	11.139	10.838

eigendecomposition of \mathbf{L}_{sym} then provides the orthogonal graph spectral basis used to construct the generalized transform basis \mathcal{F} . In this way, all compared methods are evaluated on the same graph topology and differ only in the adopted transform/filter design.

Setup: To construct the data samples, we extract the first 1500 temporal observations from each dataset. The truncated temporal sequence is then reshaped into graph signal snapshots and split chronologically into training, validation, and testing subsets with a ratio of 60%, 20%, and 20%, respectively. All models are trained using Adam with an initial learning rate of 0.001 and weight decay of 0.001. The optimization objective is the MSE loss. We train for at most 500 epochs, reduce the learning rate by a factor of 0.5 when the validation loss does not improve for 10 epochs, and employ early stopping with a patience of 30 epochs. The model achieving the lowest validation loss is restored for testing, and the final reconstruction quality is reported in terms of SNR on the unseen test set.

To highlight the benefit of our proposed NOFF mechanism, we organize the baselines into matched pairs. Specifically, global fractional filtering (GFF) methods share a single common filter across the entire graph, whereas NOFF methods assign an independent spectral filtering response to each node. This paired design allows us to isolate the performance gain brought by the node-oriented spatial adaptation from the gain brought by the fractional transform family itself. For fair comparison, all methods are initialized under the same principle. The filter matrix is initialized as an all-ones matrix. For GFRFT-based methods, the fractional order is initialized as $\alpha = 1$. For MPGFRFT-based methods, the order vector is initialized as $\mathbf{a} = (1, 1, \dots, 1)$. Table III first compares global and node-oriented filtering under several fractional-domain transforms, including GFRFT, MPGFRFT-I, MPGFRFT-II, Lap-GLCT and wAdj-GLCT. For simplicity of presentation in the tables, we abbreviate the global and node-oriented variants of a specific transform as GFF-[Transform] and NOFF-[Transform], respectively. It is evident that the node-oriented methods consistently outperform their global counterparts across all evaluated fractional domains. This performance gap strongly validates the necessity of our proposed node-level spatial adaptation. It fully unleashes the potential of fractional transforms, allowing for localized and proactive spectral modulation that a globally shared filter is fundamentally incapable of achieving.

To provide deeper physical insights into the superior performance of the NOFF framework, we visualize the learned spectral filters and fractional parameters. All visualizations are extracted from the first layer of the models evaluated on the Exchange-rate dataset

under a noise level of $\sigma = 0.5$. Fig. 3 illustrates the 3D surfaces of the learned filters across five fractional domains. In the top row, the GFF-methods exhibit invariant spectral responses along the vertex index axis, confirming that a rigid, one-size-fits-all profile is enforced across the entire graph. In stark contrast, the bottom row reveals that the proposed NOFF framework generates highly rugged and localized filter surfaces. The spectral response dynamically adapts to the specific local topological environment of each vertex, providing compelling visual evidence for the necessity of node-oriented spatial adaptation. Fig. 4 plots the distribution of the optimized fractional parameters. Fig. 4(a) shows the learned orders for GFRFT and MPGFRFT variants. It is evident that all learned parameters systematically deviate from the standard GFT domain ($\alpha = 1.0$). Notably, the MPGFRFT variants assign highly distinctive fractional orders to individual vertices, fully exploiting their multi-parameter degrees of freedom. Similarly, Fig. 4(b) demonstrates that the learned phase parameters (a, b, d) for the GLCT variants also converge to non-trivial optimal values. These parameter deviations provide explicit empirical validation that our framework successfully locates an optimal intermediate transform space, thereby decoupling complex noise components that remain severely entangled in the standard spectral domain.

To further demonstrate the superiority of the proposed framework, we extract the best-performing node-oriented configurations from the fractional domains (i.e., the optimal variants from GFRFT, MPGFRFT, and GLCT) and compare them against the node-oriented GFT (NO-GFT) filter as well as several state-of-the-art GNN and graph transformer methods. As reported in Table IV, the proposed NOFF methods demonstrate a clear and consistent advantage over the NO-GFT approach across all evaluated scenarios. This observation perfectly corroborates our theoretical motivation: although the node-oriented GFT introduces spatial adaptability, its reliance on the rigidly fixed standard spectral domain restricts its capacity to decouple the true signal from complex noise. In contrast, the fractional domains provide crucial extra degrees of freedom, enabling proactive spectral modulation to separate aliased frequency components. Meanwhile, they also achieve stronger denoising performance than the considered neural baselines, further confirming the effectiveness and competitiveness of the proposed fractional-domain framework.

B. Experiments on large-scale graphs

Datasets and Graph Construction: To evaluate the scalability and denoising performance of the proposed LRNOFF mechanism

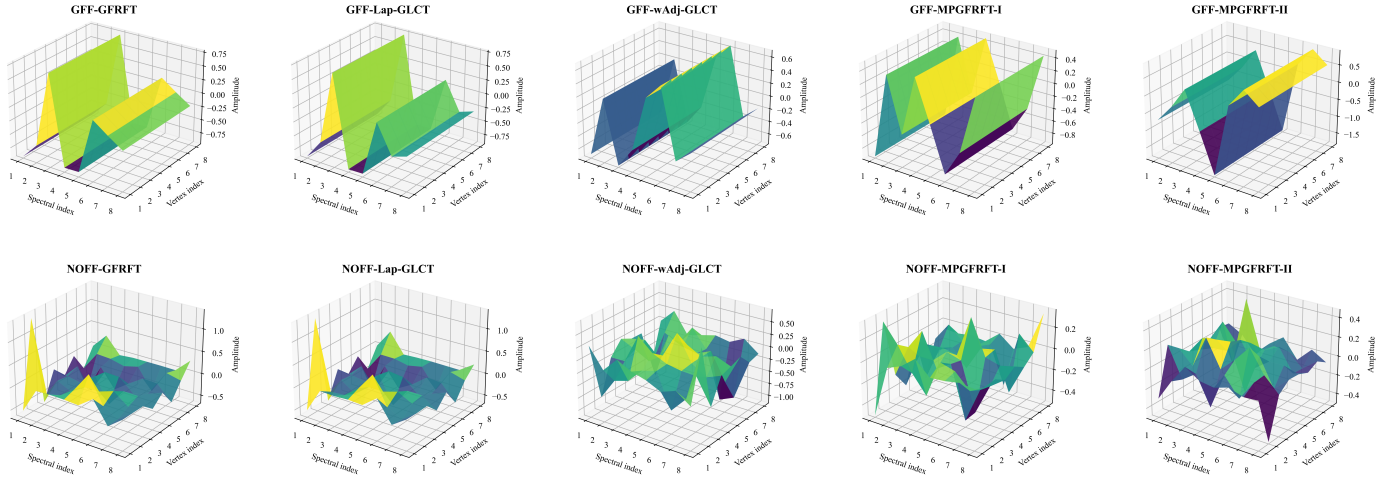


Fig. 3: Visualization of the learned 3D filter surfaces on the Exchange-rate dataset ($\sigma = 0.5$, Layer 1).

TABLE IV: Denoising performance comparison of NOFF and state-of-the-art baselines on small-scale datasets.

Dataset	Quality				Exchange-rate			
	50	80	150	200	0.5	0.8	1	1.2
σ								
SNR	3.949	-0.133	-5.593	-8.092	4.209	0.126	-1.812	-3.395
APPNP	7.078	4.963	3.521	3.250	7.781	6.179	5.728	5.466
GAT	7.088	4.996	3.578	3.268	7.542	6.070	5.644	5.409
GCN	7.006	4.945	3.527	3.254	7.626	6.111	5.678	5.432
H2GCN	8.180	5.984	3.815	3.159	7.757	5.888	5.252	4.857
ChebyNet	7.120	5.013	3.560	3.265	7.942	6.315	5.855	5.582
BernNet	6.761	4.446	2.693	2.259	6.698	4.701	4.052	3.637
GPR-GNN	8.111	5.950	3.770	3.307	9.363	7.571	7.015	6.689
ARMAConv	7.133	5.019	3.591	3.279	7.815	6.221	5.764	5.497
SpecFormer	7.516	5.768	4.416	4.079	10.436	9.269	8.924	8.717
UniMP	7.114	5.028	3.550	3.279	7.882	6.294	5.838	5.559
PolyFormer	7.619	5.244	3.711	3.199	7.389	5.970	5.567	5.340
NO-GFT	10.425	8.124	5.833	5.119	12.879	10.927	10.270	10.017
NOFF-GFRFT	10.616	8.388	6.045	5.410	13.202	11.478	10.940	10.657
NOFF-MPGFRFT	10.604	8.376	5.930	5.388	13.929	11.864	11.420	10.991
NOFF-GLCT	10.513	8.336	5.994	5.428	13.442	11.512	11.139	10.838

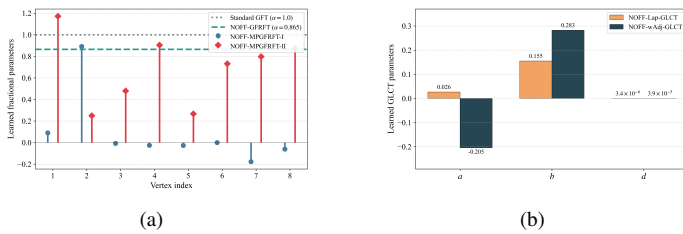


Fig. 4: Distribution of the optimized fractional parameters on the Exchange-rate dataset ($\sigma = 0.5$, Layer 1). (a) Learned parameters for GFRFT and MPGFRFT variants. (b) Learned phase parameters (a, b, d) for GLCT variants.

on large-scale networks, we conduct experiments on four widely-used real-world spatiotemporal datasets: METR ($N = 207$), PEMS08 ($N = 170$) [37]–[39], Solar ($N = 137$) [40] and Electricity ($N = 370$) [41]. Specifically, to ensure temporally aligned dense observations for the Electricity dataset, we truncate the initial inactive periods and construct a symmetric 5-nearest neighbor (5-NN) graph based on the Pearson correlation of average daily load profiles. For the Solar dataset, lacking spatial coordinates,

its symmetric 5-NN graph topology is similarly built using the positive Pearson correlations of the full time series. Finally, for all datasets, the graph shift operator and the corresponding generalized transform bases are constructed using the same normalized symmetric Laplacian method detailed in Section V-A.

Setup: To ensure a fair comparison and maintain consistency throughout our study, the experimental configurations for LRNOFF-Fast, including the data splitting ratio, optimizer settings (learning rate and weight decay), and early stopping criteria, are kept identical to those specified for the NOFF in Section V-A. For the low-rank filter dictionary, to prevent the decomposed sub-filters from converging to identical states while preserving the initial all-pass property, we initialize the parameter matrices with microscopic Gaussian noise. Specifically, the base spectral matrix $\mathbf{B} \in \mathbb{R}^{d \times N}$ and the weight matrix $\mathbf{W} \in \mathbb{R}^{N \times d}$ are initialized with independent and identically distributed (i.i.d.) samples as $B_{k,j} \sim \mathcal{N}(1.0, 0.1^2)$ and $W_{i,k} \sim \mathcal{N}(1/d, 0.01^2)$, respectively.

To demonstrate the necessity and superiority of the low-rank approximation, Table V compares the GFF mechanism and our proposed LRNOFF-Fast across various fractional domains, including GFRFT, MPGFRFT-I, MPGFRFT-II, Lap-GLCT, and wAdj-GLCT.

TABLE V: Denoising performance comparison of GFF-based and LRNOFF-Fast-based methods under various low-rank dimensions d on large-scale datasets.

Dataset	METR			PEMS08			Solar			Electricity			
	σ	40	60	80	100	150	200	8	10	12	3000	5000	6000
SNR	3.495	-0.027	-2.526	8.006	4.485	1.986		1.486	-0.452	-2.036	4.089	-0.348	-1.932
$d = 3$													
GFF-GFRFT	14.732	13.998	13.439	15.374	14.997	14.478	12.210	11.677	11.249	22.306	20.259	19.106	
LRNOFF-Fast-GFRFT	15.960	14.628	13.862	17.931	15.688	15.438	13.306	12.843	12.201	24.256	21.465	20.510	
GFF-MPGFRFT-I	15.257	14.236	13.426	16.724	15.566	14.844	12.148	11.418	10.882	23.580	20.755	19.906	
LRNOFF-Fast-MPGFRFT-I	15.790	14.565	13.792	18.165	15.964	15.614	13.311	12.633	12.171	24.352	21.544	20.534	
GFF-MPGFRFT-II	14.819	13.796	13.319	16.326	15.104	14.438	11.934	11.504	11.365	23.733	21.030	20.097	
LRNOFF-Fast-MPGFRFT-II	15.803	14.433	13.749	18.208	16.696	15.654	13.577	12.714	11.763	24.242	21.543	20.521	
GFF-Lap-GLCT	14.728	14.001	13.416	14.897	13.916	14.484	12.987	11.685	11.319	18.252	17.841	19.109	
LRNOFF-Fast-Lap-GLCT	15.797	14.647	13.844	17.955	16.387	15.443	13.323	12.580	12.216	24.200	21.413	20.471	
GFF-wAdj-GLCT	14.406	13.594	13.007	14.688	13.832	13.178	11.075	10.284	9.738	23.151	20.467	19.501	
LRNOFF-Fast-wAdj-GLCT	15.763	14.460	13.604	17.864	16.334	15.671	13.348	12.534	12.033	23.763	21.239	20.296	
$d = 5$													
GFF-GFRFT	14.732	13.998	13.439	15.374	14.997	14.478	12.210	11.677	11.249	22.306	20.259	19.106	
LRNOFF-Fast-GFRFT	16.115	14.656	13.794	18.258	16.063	15.930	13.520	12.738	12.090	24.323	21.569	20.554	
GFF-MPGFRFT-I	15.257	14.236	13.426	16.724	15.566	14.844	12.148	11.418	10.882	23.580	20.755	19.906	
LRNOFF-Fast-MPGFRFT-I	15.907	14.563	13.781	18.430	16.522	15.933	13.639	12.599	11.943	24.416	21.581	20.646	
GFF-MPGFRFT-II	14.819	13.796	13.319	16.326	15.104	14.438	11.934	11.504	11.365	23.733	21.030	20.097	
LRNOFF-Fast-MPGFRFT-II	15.954	14.529	13.787	18.331	16.628	15.877	13.301	12.464	12.009	24.336	21.588	20.462	
GFF-Lap-GLCT	14.728	14.001	13.416	14.897	13.916	14.484	12.987	11.685	11.319	18.252	17.841	19.109	
LRNOFF-Fast-Lap-GLCT	15.842	14.594	13.789	18.267	16.399	15.930	13.502	12.694	12.102	24.437	21.545	20.567	
GFF-wAdj-GLCT	14.406	13.594	13.007	14.688	13.832	13.178	11.075	10.284	9.738	23.151	20.467	19.501	
LRNOFF-Fast-wAdj-GLCT	15.764	14.415	13.596	18.125	16.062	15.697	13.552	12.754	12.131	24.030	21.219	20.311	
$d = 10$													
GFF-GFRFT	14.732	13.998	13.439	15.374	14.997	14.478	12.210	11.677	11.249	22.306	20.259	19.106	
LRNOFF-Fast-GFRFT	16.070	14.620	13.810	18.493	16.119	15.914	13.365	12.665	12.112	24.329	21.387	20.374	
GFF-MPGFRFT-I	15.257	14.236	13.426	16.724	15.566	14.844	12.148	11.418	10.882	23.580	20.755	19.906	
LRNOFF-Fast-MPGFRFT-I	15.906	14.575	13.796	18.502	16.553	15.893	13.241	12.494	11.944	24.313	21.624	20.622	
GFF-MPGFRFT-II	14.819	13.796	13.319	16.326	15.104	14.438	11.934	11.504	11.365	23.733	21.030	20.097	
LRNOFF-Fast-MPGFRFT-II	15.816	14.434	13.655	18.395	16.520	15.926	13.613	12.593	11.708	24.292	21.609	20.518	
GFF-Lap-GLCT	14.728	14.001	13.416	14.897	13.916	14.484	12.987	11.685	11.319	18.252	17.841	19.109	
LRNOFF-Fast-Lap-GLCT	16.113	14.647	13.806	18.427	16.412	15.882	13.600	12.675	12.106	24.233	21.472	20.456	
GFF-wAdj-GLCT	14.406	13.594	13.007	14.688	13.832	13.178	11.075	10.284	9.738	23.151	20.467	19.501	
LRNOFF-Fast-wAdj-GLCT	15.812	14.423	13.616	18.358	16.247	15.838	13.586	12.698	12.066	24.245	21.265	20.262	
$d = 15$													
GFF-GFRFT	14.732	13.998	13.439	15.374	14.997	14.478	12.210	11.677	11.249	22.306	20.259	19.106	
LRNOFF-Fast-GFRFT	15.945	14.553	13.788	18.577	16.095	15.950	13.319	12.520	12.091	24.220	21.341	20.402	
GFF-MPGFRFT-I	15.257	14.236	13.426	16.724	15.566	14.844	12.148	11.418	10.882	23.580	20.755	19.906	
LRNOFF-Fast-MPGFRFT-I	15.944	14.512	13.780	18.559	16.535	15.987	13.423	12.663	12.122	24.217	21.493	20.460	
GFF-MPGFRFT-II	14.819	13.796	13.319	16.326	15.104	14.438	11.934	11.504	11.365	23.733	21.030	20.097	
LRNOFF-Fast-MPGFRFT-II	15.865	14.380	13.713	18.524	16.714	15.723	13.429	12.523	11.889	24.255	21.426	20.390	
GFF-Lap-GLCT	14.728	14.001	13.416	14.897	13.916	14.484	12.987	11.685	11.319	18.252	17.841	19.109	
LRNOFF-Fast-Lap-GLCT	16.018	14.517	13.800	18.549	16.107	15.961	13.316	12.361	11.955	24.243	21.430	20.372	
GFF-wAdj-GLCT	14.406	13.594	13.007	14.688	13.832	13.178	11.075	10.284	9.738	23.151	20.467	19.501	
LRNOFF-Fast-wAdj-GLCT	15.744	14.435	13.655	18.340	15.981	15.809	13.563	12.705	12.066	24.224	21.346	20.401	

As shown in Table V, the LRNOFF-Fast consistently and substantially outperforms the GFF counterparts. This observation not only verifies that our low-rank decomposition successfully breaks the curse of dimensionality, but also provides strong empirical evidence that node-oriented adaptation is fundamentally superior to traditional global filtering. By assigning customized spectral responses to individual vertices, the node-oriented mechanism effectively overcomes the rigid, one-size-fits-all limitation of global filters.

Following the quantitative results in Table V, we provide visualizations to demonstrate how the LRNOFF-Fast mechanism efficiently distills complex spectral responses into a compact yet expressive subspace.

1) Effectiveness of low-rank factorization: First, we visualize

the learned decomposition components (\mathbf{W} and \mathbf{B}) alongside the reconstructed full filter ($\mathbf{H} = \mathbf{WB}$) on the Solar dataset with a rank of $d = 3$. As illustrated in Fig. 5, learning \mathbf{W} and \mathbf{B} circumvents the prohibitive $\mathcal{O}(N^2)$ parameter explosion associated with the full filter \mathbf{H} . Despite the extreme dimensional compression ($d \ll N$), the reconstructed \mathbf{H} continues to exhibit highly intricate, localized, and domain-specific structural patterns across different fractional transforms. This proves that the low-rank factorization effectively resolves the curse of dimensionality without sacrificing the rich spatial-spectral interactions required for large-scale graphs.

2) Spatial interpretability of the latent subspace: Second, we map the learned spatial weight matrix \mathbf{W} onto the physical geographic space. Using the METR dataset, Fig. 6 illustrates the spatial activation amplitudes of the three latent basis components ($\mathbf{w}_1, \mathbf{w}_2, \mathbf{w}_3$).

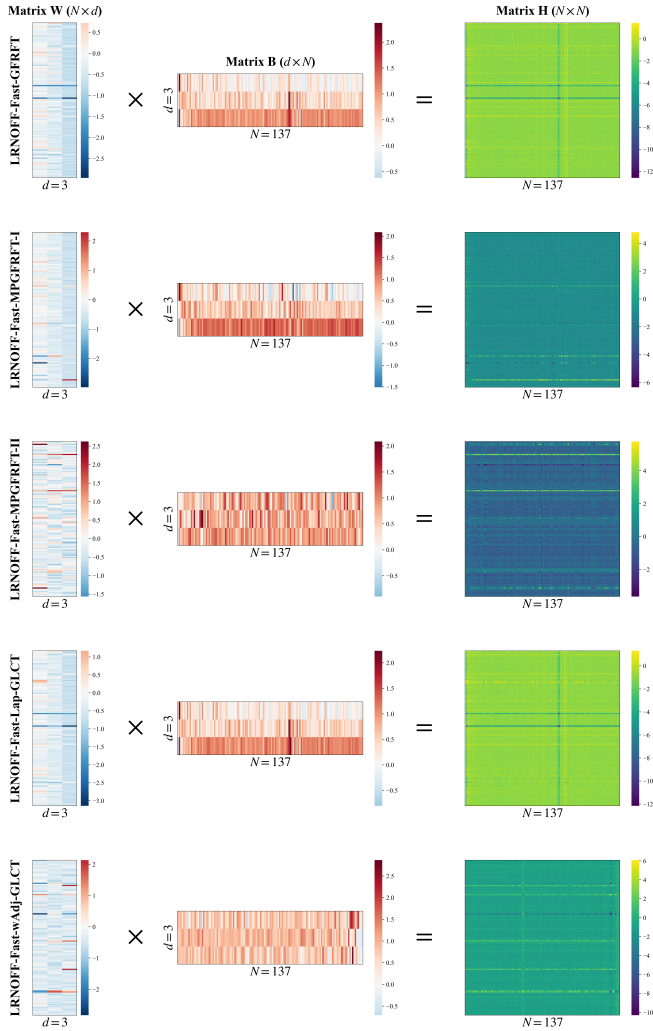


Fig. 5: Visualizations of the learned low-rank components on the Solar dataset across various fractional domains.

The visualization reveals a clear separation of spatial functional modes: w_2 exhibits a relatively uniform distribution capturing the global low-frequency trend; w_1 displays distinct regional clustering extracting regional structural features; and w_3 presents rapid spatial variations around complex intersections, acting as a local bottleneck mode. This indicates that the LRNOFF framework successfully learns physically meaningful spatial receptive fields purely driven by data.

3) Data-driven adaptation of the fractional spectral domains: Finally, to demonstrate how our framework adaptively optimizes the spectral representation, we visualize the learned fractional parameters across five specific transform variants (Fig. 7). The results reveal that the optimized parameter sets diverge significantly from the standard Fourier domain ($\alpha = 1$). This substantial deviation confirms that our framework effectively transforms the graph spectrum into an optimal fractional domain, maximizing the separation of complex signal and noise representations prior to applying the node-specific filters constructed from a shared set of latent bases.

Furthermore, to comprehensively evaluate the superiority of our framework on large-scale graphs, we extract the best-performing LRNOFF-Fast configurations from the fractional domains specifically under the low-rank subspace dimension of $d = 15$. These optimal variants are then compared against the LRNO-GFT as well

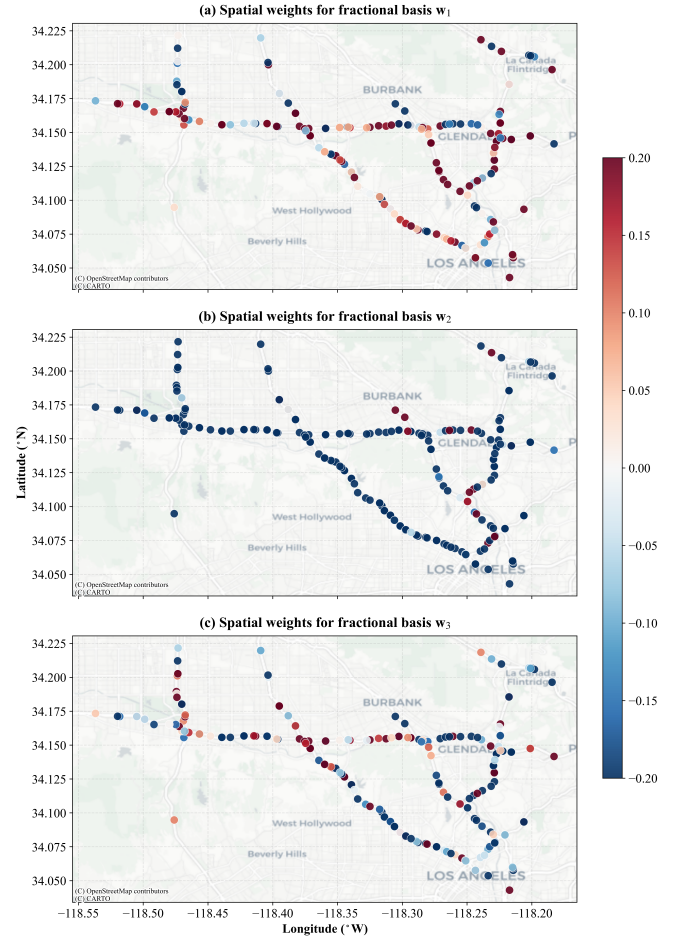


Fig. 6: Geographic mapping of the learned spatial weights for the three fractional bases (w_1, w_2, w_3) on the METR road network.

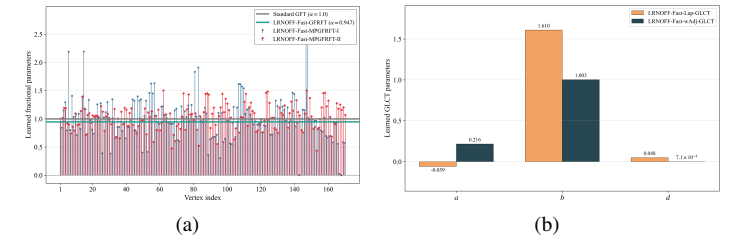


Fig. 7: Distribution of the optimized fractional parameters on the PEMS08 dataset ($\sigma = 150$, Layer 2). (a) Learned parameters for GFRFT and MPGRFT variants. (b) Learned phase parameters (a, b, d) for GLCT variants.

as several state-of-the-art neural network baselines. As reported in Table VI, with the minor exception of a performance tie between LRNOFF-Fast-GFRFT and LRNO-GFT on the Electricity dataset ($\sigma = 3000$), the proposed fractional methods exhibit a clear and consistent advantage over the standard GFT approach across all other evaluated scenarios. As previously observed in the small-graph scenarios, the standard GFT suffers from spectral rigidity. This limitation is amplified on massive graphs, where signal components and complex noise patterns are more densely packed. The fractional domains successfully resolve this bottleneck by utilizing their dynamically learned parameters to map the entangled graph signals into an optimal transform space for cleaner separation. Most importantly, our LRNOFF-Fast achieves stronger denoising performance than the neural baselines, perfectly highlighting its

TABLE VI: Denoising performance comparison of LRNOFF-Fast ($d = 15$) and state-of-the-art baselines on large-scale datasets.

Dataset	METR			PEMS08			Solar			Electricity		
	40	60	80	100	150	200	8	10	12	3000	5000	6000
σ	3.495	-0.027	-2.526	8.006	4.485	1.986	1.486	-0.452	-2.036	4.089	-0.348	-1.932
SNR												
APPNP	12.419	11.974	11.831	10.037	7.968	6.920	5.705	4.493	3.665	13.855	11.180	5.097
GAT	12.626	12.139	11.984	9.939	7.965	6.945	5.768	4.570	3.752	10.683	9.272	8.252
GCN	12.402	11.947	11.807	9.865	7.893	6.889	5.673	4.472	3.657	10.154	8.850	8.305
H2GCN	12.329	11.547	11.144	10.622	8.805	7.780	8.303	7.394	6.697	9.008	5.577	4.515
Chebynet	12.577	12.120	11.959	10.131	8.065	7.015	5.835	4.629	3.804	14.118	11.323	10.177
Bern	6.080	5.001	4.658	9.407	6.955	5.567	5.349	4.198	3.415	7.955	4.745	3.865
GPR-GNN	13.033	12.138	11.787	10.838	9.047	8.105	8.970	8.025	7.301	14.277	11.423	10.456
ARMAcov	12.615	12.110	11.983	10.103	8.040	6.998	5.828	4.613	3.792	13.902	11.360	10.245
Specformer	12.575	12.205	12.143	11.176	9.632	8.853	5.370	4.481	3.671	7.837	5.626	5.055
Unimp	12.615	12.110	11.902	10.089	8.028	6.986	5.816	4.601	3.790	14.044	11.256	3.875
Polyformer	13.221	12.470	12.207	7.225	6.344	5.954	9.662	8.631	7.500	13.841	11.562	10.564
LRNO-Fast-GFT	15.918	14.416	13.647	18.545	15.765	15.907	13.179	12.209	11.642	24.220	21.315	20.394
LRNOFF-Fast-GFRFT	15.945	14.553	13.788	18.577	16.095	15.950	12.210	11.677	11.249	24.220	21.341	20.402
LRNOFF-Fast-MPGFRFT	15.944	14.512	13.780	18.559	16.714	15.987	13.429	12.663	12.122	24.255	21.493	20.460
LRNOFF-Fast-GLCT	16.018	14.517	13.800	18.549	16.107	15.961	13.563	12.705	12.066	24.243	21.430	20.401

remarkable efficiency, anti-overfitting capability, and mathematical interpretability in processing large-scale graph signals.

VI. CONCLUSION

In this paper, we addressed the fundamental dilemma between spatial adaptability and spectral flexibility in graph signal denoising by proposing a generalized NOFF framework. By introducing node-wise spectral modulation into fractional-domain transforms, NOFF effectively overcomes both the spectral rigidity of the standard node-oriented method and the spatial limitations of globally shared fractional filters. To resolve the catastrophic parameter explosion and noise memorization issues inherent in unconstrained local filtering, we introduced the LRNOFF architecture. Our analysis reveals that imposing a strict low-rank constraint on the ideal localized filter matrix acts as a powerful implicit regularizer, effectively forcing the network to learn robust, physically meaningful spectral bases instead of fitting high-frequency random noise. Moreover, the development of LRNOFF-Fast successfully translates this theoretical optimality into an efficient computational approach for large-scale real-world networks. Empirical results validate the superiority of our framework over existing graph filters and advanced graph neural networks.

APPENDIX A

PROOF OF THEOREM 1

Substituting the low-rank constraint (24) into (17), we have

$$\tilde{x}_i = \sum_{j=1}^N \mathcal{F}_{i,j}^{-1} \left(\sum_{k=1}^d W_{i,k} B_{k,j} \right) (\mathcal{F}\mathbf{x})_j. \quad (36)$$

Utilizing the commutative property of linear summation, we swap the order of operations

$$\tilde{x}_i = \sum_{k=1}^d W_{i,k} \left(\sum_{j=1}^N \mathcal{F}_{i,j}^{-1} B_{k,j} (\mathcal{F}\mathbf{x})_j \right). \quad (37)$$

Let the inner summation be denoted as the i -th element of an intermediate vector $\mathbf{u}_k \in \mathbb{C}^N$. This inner term represents the k -th base filtered signal mapped back to the vertex domain:

$$\begin{aligned} U_{i,k} &= (\mathbf{u}_k)_i = \sum_{j=1}^N \mathcal{F}_{i,j}^{-1} [B_{k,j} (\mathcal{F}\mathbf{x})_j] \\ &= (\mathcal{F}^{-1}(\mathbf{b}_k \odot \mathcal{F}\mathbf{x}))_i. \end{aligned} \quad (38)$$

Subsequently, the outer summation in (37) degrades into a localized spatial weighting of the d base signals in the vertex domain

$$\tilde{x}_i = \sum_{k=1}^d W_{i,k} U_{i,k}. \quad (39)$$

By vectorizing this operation across all vertices i , the global filtered signal is exactly expressed as $\tilde{\mathbf{x}} = \sum_{k=1}^d \mathbf{w}_k \odot \mathbf{u}_k$, which completes the proof. ■

APPENDIX B

PROOF OF THEOREM 2

The filtering output at vertex i can be expressed as the inner product

$$\tilde{x}_i = (\mathbf{w}^{(i)})^\top \mathbf{u}^{(i)}. \quad (40)$$

Expanding the MSE cost function $J(\mathbf{w}^{(i)}) = \mathbb{E}[|\tilde{x}_i - x_i|^2]$ and setting the partial derivative with respect to $\mathbf{w}^{(i)}$ to zero yields

$$\mathbb{E} \left[(\mathbf{u}^{(i)})^* (\mathbf{u}^{(i)})^\top \right] \mathbf{w}^{(i)} = \mathbb{E} \left[(\mathbf{u}^{(i)})^* x_i \right]. \quad (41)$$

Solving this equation directly yields the closed-form Wiener solution, which completes the proof. ■

APPENDIX C

PROOF OF THEOREM 3

Given the fixed \mathbf{W} , the k -th base signal is $\mathbf{u}_k = \Psi \mathbf{b}^{(k)}$. The output at node i can be written as

$$\tilde{x}_i = \sum_{k=1}^d W_{i,k} \Psi_{i,:} \mathbf{b}^{(k)}. \quad (42)$$

Utilizing the concatenated definition, this simplifies to the inner product $\tilde{x}_i = \mathbf{v}^{(i)} \mathbf{b}$. Expanding the global MSE cost function $J(\mathbf{b})$ and setting the partial derivative with respect to \mathbf{b} to zero yields

$$\left(\sum_{i=1}^N \mathbb{E} [(\mathbf{v}^{(i)})^H \mathbf{v}^{(i)}] \right) \mathbf{b} = \sum_{i=1}^N \mathbb{E} [x_i (\mathbf{v}^{(i)})^H]. \quad (43)$$

By substituting the definitions of the global auto-correlation matrix \mathbf{R}_V and the global cross-correlation vector \mathbf{r}_{Vx} , the closed-form global Wiener solution is directly obtained. ■

APPENDIX D
PROOF OF THEOREM 4

According to the Eckart-Young-Mirsky theorem, the closest rank- d approximation of any matrix in the Frobenius norm is strictly achieved by truncating its SVD to the principal d components, yielding $\mathbf{H}_d^* = \mathbf{U}_d \mathbf{\Sigma}_d \mathbf{V}_d^H$. By introducing the symmetric splitting of the diagonal singular value matrix $\mathbf{\Sigma}_d = \mathbf{\Sigma}_d^{1/2} \mathbf{\Sigma}_d^{1/2}$, the optimal low-rank matrix can be rewritten as $\mathbf{H}_d^* = (\mathbf{U}_d \mathbf{\Sigma}_d^{1/2})(\mathbf{\Sigma}_d^{1/2} \mathbf{V}_d^H)$. Substituting the definitions of \mathbf{W}_{opt} and \mathbf{B}_{opt} directly yields $\mathbf{H}_d^* = \mathbf{W}_{opt} \mathbf{B}_{opt}$, which completes the proof. ■

REFERENCES

- [1] A. Ortega, P. Frossard, J. Kovacevic, J. M. F. Moura, and P. Vandergheynst, "Graph signal processing: Overview, challenges, and applications," *Proc. IEEE*, vol. 106, no. 5, pp. 808–828, Apr. 2018.
- [2] A. Ortega, *Introduction to Graph Signal Processing*. Cambridge University Press, 2022.
- [3] J. L. Wang, R. Gao, H. T. Zheng, H. Zhu, and C.-J. R. Shi, "SSGCNet: A sparse spectra graph convolutional network for epileptic EEG signal classification," *IEEE Trans. Neural Netw. Learn. Syst.*, vol. 35, no. 9, pp. 12 157–12 171, Mar. 2024.
- [4] R. Li, X. Yuan, M. Radfar, P. Marendy, W. Ni, T. J. O'Brien, and P. M. Casillas-Espinosa, "Graph signal processing, graph neural network and graph learning on biological data: A systematic review," *IEEE Rev. Biomed. Eng.*, vol. 16, pp. 109–135, Dec. 2023.
- [5] X. Y. Song, K. Wu, and L. Chai, "Brain network analysis of schizophrenia patients based on hypergraph signal processing," *IEEE Trans. Image Process.*, vol. 32, pp. 4964–4976, Aug. 2023.
- [6] Q. Bao, B. Gang, W. Yang, J. Zhou, and Q. Liao, "Attention-driven graph neural network for deep face super-resolution," *IEEE Trans. Image Process.*, vol. 31, pp. 6455–6470, Oct. 2022.
- [7] G. G. Dong, H. W. Liu, G. Y. Kuang, and J. Chanussot, "Target recognition in SAR images via sparse representation in the frequency domain," *Pattern Recognit.*, vol. 96, p. 106972, Dec. 2019.
- [8] S. S. Saboksayr, G. Mateos, and M. Cetin, "EEG-based emotion classification using graph signal processing," in *Proc. IEEE International Conference on Acoustics, Speech and Signal Processing (ICASSP)*, Jun. 2021, pp. 1065–1069.
- [9] Y. Ma, X. R. Liu, T. Zhao, Y. Z. Liu, J. L. Tang, and N. Shah, "A unified view on graph neural networks as graph signal denoising," in *Proc. ACM International Conference on Information and Knowledge Management (CIKM)*, Oct. 2021, pp. 1202–1211.
- [10] M. Onuki, S. Ono, M. Yamagishi, and Y. Tanaka, "Graph signal denoising via trilateral filter on graph spectral domain," *IEEE Trans. Signal Inf. Process. Netw.*, vol. 2, no. 2, pp. 137–148, Feb. 2016.
- [11] S. H. Chen, Y. C. Eldar, and L. X. Zhao, "Graph unrolling networks: Interpretable neural networks for graph signal denoising," *IEEE Trans. Signal Process.*, vol. 69, pp. 3699–3713, Jun. 2021.
- [12] A. C. Yagan and M. T. Ozgen, "Spectral graph based vertex-frequency wiener filtering for image and graph signal denoising," *IEEE Trans. Signal Inf. Process. Netw.*, vol. 6, pp. 226–240, Feb. 2020.
- [13] A. Sandryhaila and J. M. F. Moura, "Discrete signal processing on graphs," *IEEE Trans. Signal Process.*, vol. 61, no. 7, pp. 1644–1656, Jan. 2013.
- [14] J. Domingos and J. M. F. Moura, "Graph Fourier transform: A stable approximation," *IEEE Trans. Signal Process.*, vol. 68, pp. 4422–4437, Jul. 2020.
- [15] W. F. Qi, S. R. Guo, and W. Hu, "Generic reversible visible watermarking via regularized graph Fourier transform coding," *IEEE Trans. Image Process.*, vol. 31, pp. 691–705, Dec. 2022.
- [16] A. C. Yagan and M. T. Ozgen, "A spectral graph wiener filter in graph Fourier domain for improved image denoising," in *Proc. IEEE Global Conference on Signal and Information Processing (GlobalSIP)*, Apr. 2016, pp. 450–454.
- [17] S. Zheng, Z. F. Zhu, Z. Z. Liu, Y. R. Li, and Y. Zhao, "Node-oriented spectral filtering for graph neural networks," *IEEE Trans. Pattern Anal. Mach. Intell.*, vol. 46, no. 1, pp. 388–402, Oct. 2024.
- [18] J. Y. Chen, B. Z. Li, and L. Peng, "Hyper-differential operator-based graph fractional Fourier transform: Novel approaches and applications," *IEEE Trans. Signal Inf. Process. Netw.*, vol. 12, pp. 411–423, Mar. 2026.
- [19] Y. Q. Wang and B. Z. Li, "The fractional Fourier transform on graphs: Sampling and recovery," in *Proc. 14th IEEE International Conference on Signal Processing (ICSP)*, Aug. 2018, pp. 1103–1108.
- [20] C. Ozturk, H. M. Ozaktas, S. Gezici, and A. Koç, "Optimal fractional Fourier filtering for graph signals," *IEEE Trans. Signal Process.*, vol. 69, pp. 2902–2912, May 2021.
- [21] Y. C. Gan, J. Y. Chen, and B. Z. Li, "The windowed two-dimensional graph fractional Fourier transform," *Digit. Signal Process.*, vol. 162, p. 105191, Jul. 2025.
- [22] T. Alikasifoglu, B. Kartal, and A. Koc, "Wiener filtering in joint time-vertex fractional Fourier domains," *IEEE Signal Process. Lett.*, vol. 31, pp. 1319–1323, May 2024.
- [23] M. J. Cui, Z. C. Zhang, and W. Yao, "Multiple-parameter graph fractional Fourier transform: Theory and applications," *arXiv preprint arXiv:2507.23570*, 2025.
- [24] N. Li and Z. C. Zhang, "Multi-dimensional graph linear canonical transform," *Digit. Signal Process.*, vol. 165, p. 105334, Oct. 2025.
- [25] J. Y. Chen, Y. Zhang, and B. Z. Li, "Graph linear canonical transform: Definition, vertex-frequency analysis and filter design," *IEEE Trans. Signal Process.*, vol. 72, pp. 5691–5707, Dec. 2024.
- [26] Y. Zhang and B. Z. Li, "Discrete linear canonical transform on graphs," *Digit. Signal Process.*, vol. 135, p. 103934, Apr. 2023.
- [27] F. J. Yan and B. Z. Li, "Multi-dimensional graph fractional Fourier transform and its application to data compression," *Digit. Signal Process.*, vol. 129, p. 103683, Sep. 2022.
- [28] —, "Windowed fractional Fourier transform on graphs: Properties and fast algorithm," *Digit. Signal Process.*, vol. 118, p. 103210, Nov. 2021.
- [29] T. Alikasifoglu, B. Kartal, E. Ozgunay, and A. Koc, "Joint time-vertex fractional Fourier transform," *Signal Process.*, vol. 233, p. 109944, Aug. 2025.
- [30] T. Alikasifoglu, B. Kartal, and A. Koc, "Graph fractional Fourier transform: A unified theory," *IEEE Trans. Signal Process.*, vol. 72, pp. 3834–3850, Aug. 2024.
- [31] C. C. Tseng and S. L. Lee, "A graph signal denoising method using total variation regularization and fractional graph Fourier transform," in *Proc. International Symposium on Intelligent Signal Processing and Communication Systems (ISPACS)*, Dec. 2024, pp. 1–5.
- [32] —, "A fractional graph Fourier transform method for missing data recovery of sensor network," in *Proc. Global Conference on Consumer Electronics (GCCE)*, Oct. 2024, pp. 154–155.
- [33] R. Li, X. Yuan, M. Radfar, P. Marendy, W. Ni, T. J. O'Brien, and P. M. Casillas-Espinosa, "Graph signal processing, graph neural network and graph learning on biological data: A systematic review," *IEEE Rev. Biomed. Eng.*, vol. 16, pp. 109–135, Oct. 2023.
- [34] Y. Q. Wang, B. Z. Li, and Q. Y. Cheng, "The fractional Fourier transform on graphs," in *Proc. Asia-Pacific Signal and Information Processing Association Annual Summit and Conference (APSIPA ASC)*, Dec. 2017, pp. 105–110.
- [35] K. Yi, Q. Zhang, W. Fan, S. J. Wang, P. Y. Wang, H. He, N. An, D. F. Lian, L. B. Cao, and Z. D. Niu, "Frequency-domain MLPs are more effective learners in time series forecasting," in *Proc. Advances in Neural Information Processing Systems (NeurIPS)*, vol. 36, Dec. 2023, pp. 76 656–76 679.
- [36] G. K. Lai, W. C. Chang, Y. M. Yang, and H. X. Liu, "Modeling long- and short-term temporal patterns with deep neural networks," in *Proc. International ACM SIGIR Conference on Research and Development in Information Retrieval (SIGIR)*, Jun. 2018, pp. 95–104.
- [37] Z. Q. Yan and Z. C. Zhang, "JFRFFNet: A data-model co-driven graph signal denoising model with partial prior information," *IEEE Signal Process. Lett.*, vol. 33, pp. 1038–1042, Feb. 2026.
- [38] Y. G. Li, R. Yu, C. Shahabi, and Y. Liu, "Diffusion convolutional recurrent neural network: Data-driven traffic forecasting," in *Proc. International Conference on Learning Representations (ICLR)*, Feb. 2018.
- [39] S. N. Guo, Y. F. Lin, H. Y. Wan, X. C. Li, and G. Cong, "Learning dynamics and heterogeneity of spatial-temporal graph data for traffic forecasting," *IEEE Trans. Knowl. Data Eng.*, vol. 34, no. 11, pp. 5415–5428, Feb. 2022.
- [40] National Laboratory of the Rockies, "Solar power data for integration studies," <https://www.nrel.gov/grid/solar-power-data.html>.
- [41] G. K. Lai, W. C. Chang, Y. M. Yang, and H. X. Liu, "Modeling long- and short-term temporal patterns with deep neural networks," in *Proc. International ACM SIGIR Conference on Research & Development in Information Retrieval (SIGIR)*, Jun. 2018, pp. 95–104.